Scaling of Anode Sheath Voltage Fall with the Operational Parameters in Applied-Field MPD Thrusters

IEPC-2011-222

Presented at the 32nd International Electric Propulsion Conference,
Wiesbaden, Germany
September 11–15, 2011

Dan Lev* and Edgar Y. Choueiri †
Electric Propulsion and Plasma Dynamics Laboratory (EPPDyL)
Princeton University, Princeton, NJ, 08544, USA

Scaling laws for the anode sheath voltage fall in applied-field MPD thrusters are derived in order to better understand the physics behind anode sheath power dissipation. A semi-empirical model is formulated and verified by comparison to experimental data on a 30 kW lithium-fed steady-state AF-MPDT obtained using a hot langmuir probe. It is found that the anode sheath voltage fall increases approximately linearly with current and applied magnetic field and is inversely proportional to mass flow rate. It is shown that, although the electrons in the anode sheath are unmagnetized, the voltage fall is attributed to plasma density reduction at the sheath edge, which is a result of increased plasma pinching at higher magnitudes of applied magnetic field. It is also concluded that thermionic emission from the anode surface leads to an increase in the anode sheath voltage fall; therefore anode material with a high work function is preferred.

*Graduate Research Assistant, EPPDyL; Student Member, AIAA.
†Chief Scientist, EPPDyL; Professor, Applied Physics Group, Mechanical and Aerospace Engineering Department; Fellow AIAA.

Nomenclature

A_a	= Anode Surface Area
B	= Magnetic Field
B_c	= Applied Magnetic Field at the Cathode Exit
C_p	= Anode Material Heat Capacity
c	= Speed of Light
$\bar{E}$	= Electric Field Vector
e	= Electron Charge
f_r	= Radial Force Density
h	= Planck Constant
J	= Total Thruster Current
j_∞, j_{net}	= Net Current Density
j_e	= Electron Current Density
j_{em}	= Thermionically Emitted Electron Current Density
k_B	= Boltzmann Constant
m	= Anode Mass
m_e	= Electron Mass
$\dot{m}$	= Propellant Mass Flow Rate
n_e	= Plasma Density
P_a	= Power to Anode
r_a	= Anode Radius
T_a	= Anode Temperature
T_e	= Electron Temperature
T_i	= Ion Temperature
$\mathcal{T}$	= Thrust
$\bar{u}$	= Velocity Vector
V_a	= Anode Sheath Voltage Fall
ΔT	= Temperature Increase
Δt	= Anode Heating Time Interval
ϵ	= Emissivity
λ	= Optical Pyrometer Operational Wavelength
ν_e	= Electron Collision Frequency
ϕ_a	= Anode Material Work Function
ρ	= Mass Density
σ_0	= Scalar Conductivity
ξ	= Normalized Ionization Current
Ω_e	= Electron Hall Parameter

I. Introduction

Anode power deposition has long been identified as the main power dissipation mechanism in MPD thrusters and was shown to account for most of the thruster input power.[5,6,20,24] Since anode power fraction is high at low thruster power, low power MPD thrusters, of several hundreds of kilowatts or less, suffer from low efficiencies. Low efficiency due to anode power deposition is a common limitation in applied-field MPD (AF-MPD) thrusters since these thrusters are designed to operate at tens to hundreds of kilowatts where current is too low to generate a sufficiently high self induced field. Therefore, anode losses should be investigated and properly characterized in order to improve AF-MPD thruster efficiency.

Past experimental studies were conducted in order to characterize anode power deposition in MPD thrusters in general and AF-MPD thrusters particular. Gallimore experimentally found in self-field MPD thrusters that anode sheath voltage fall is the most significant contributor to anode power deposition.[6] He observed that an increase in thruster current leads to an increase in anode sheath voltage fall and a decrease in the anode power deposition fraction. Gallimore speculated and experimentally showed that this phenomenon is correlated with the electron Hall parameter, Ω_e, in the near anode region. However, he did not investigate the reason behind this correlation. Diamant demonstrated,[5] in self-field MPD thrusters, in the power range of 0.32-4 MW, an increase of the anode voltage fall with the normalized ionization current ($\xi \propto J/\sqrt{\dot{m}}$), which corroborates Gallimore's findings. This finding indicates that the anode voltage fall increases with increasing current and decreasing mass flow rate. In AF-MPD thrusters Myers[20] and Gallimore[19] experimentally demonstrated the anode voltage fall to be dependent on the three main operational parameters; current (J), applied magnetic field (B) and mass flow rate ($\dot{m}$). Similarly to self-field MPD thrusters, in AF-MPD thrusters, the anode fall was shown to increase with current and decreasing mass flow rate. In addition, the anode fall was shown to decrease with increasing applied magnetic field. Since the sheath size in MPD thrusters, which is of the order of a few Debye lengths ($O(10^{-6})$ m), is smaller than the electron gyro-radius, which is of the order of 10^{-4} m, the anode sheath in MPD thrusters is unmagnetized. This comes in contrast with the fact that the anode sheath fall in AF-MPD thrusters is dependent on the applied magnetic field and could not be reconciled by Myers or Gallimore.

Since anode power deposition in AF-MPD thrusters has been investigated only experimentally little is understood about the physical processes at work in the formation of the anode voltage fall and further theoretical study is needed. In addition, the experimental studies conducted by Myers and Gallimore span over a too narrow operational parameter space to draw conclusive remarks on the scaling relations of the anode voltage fall with the thruster's operational parameters. For this reason further experimental investigation, over a wide range of operational parameter space, is required.

The focus of ongoing studies on AF-MPDTs is on the most promising variant called the **Li**thium **L**orentz **F**orce **A**ccelerator (LiLFA). The LiLFA is a steady state AF-MPDT that uses lithium as a propellant and a multi-channel hollow cathode, through which the lithium vapor propellant is injected into the thruster's acceleration region. Lithium has great potential for two main reasons: 1) Lithium's first ionization potential (5.4 eV) is significantly lower than that of other, commonly-used propellants such as argon (15.7 eV), xenon (12.1 eV) or hydrogen (13.6 eV), while lithium's second ionization potential is significantly higher than that of these propellants. Therefore the frozen flow losses are expected to be lower in lithium-fed MPDTs. 2) Lithium (especially with the addition of small amounts of barium) lowers the work function of the thruster's cathode, thus enabling cathode operation at much lower temperatures[9] and reducing cathode erosion. The above two advantages make lithium a very good candidate for high power AF-MPDTs. Lithium-fed MPDTs have high efficiencies, in the range of 20% to 60% depending on the power level, and due to their low electrode erosion rate (when trace amounts of barium are added to the propellant), have demonstrated hundreds of hours of high-power operation (0.5 MW) without showing significant damage such as electrodes' erosion, cathode wear and diffusion welding of cathode end.[1,22]

The ultimate goal of this study is to find the scaling relations of the anode voltage fall with the three operational parameters; current, applied magnetic field and mass flow rate. We do so by deriving a semi-empirical model for the anode voltage fall as a function of the operational parameters, plasma properties and thruster material characteristics. The model is based on experimental measurements of the anode fall, taken on the LiLFA using a floating emissive probe, and anode temperature, by means of an optical pyrometer. Using the model we obtain physical insights on the formation of the anode sheath and explain its dependence on the operational parameters.

II. Experimental Apparatus

A. Steady State Low Power Facility

All experiments were performed in the Steady State Low Power (SSLP) facility at the Electric Propulsion and Plasma Dynamics Lab (EPPDyL) at Princeton University. The SSLP facility consists of a large cylindrical vacuum chamber, 1.5 m in diameter and 3.6 m long, made of stainless steel in order to withstand high temperatures. An active cooling jacket uses chilled water to maintain a moderate temperature along the chamber's inner walls. The ultimate vacuum of this system is 1.7×10^{-5} Torr (2.266×10^{-3} Pa) and is obtained using a 1.22 m CVC Type PMC-48C (95,000 l/s) diffusion pump, a Leybold Vacuum Products Inc. RUVAC WSU-2000 1342 CFM (630 l/s) Roots accelerator, and a 150 CFM (71 l/s) Stokes Microvac mechanical pump. All three pumps are conected to the vacuum chamber in series. Low pressure is easily kept during thruster operation since lithium is solid at room temperature and therefore condenses on the inner walls of the vacuum chamber. Therefore pressure could be kept at the ultimate pressure during firing. An ingot of about 150 g of lithium is loaded into a small stainless steel reservoir, 80 mm in diameter and 166 mm in length. We perform the loading of the reservoir under argon atmosphere in a glove box in order to keep the lithium in an inert environment. The reservoir is then attached to the thruster feeding system (Fig. 1) in the vacuum chamber, which is then closed and pumped down while a steady flow of argon in the reservoir keeps the lithium from reacting with air.

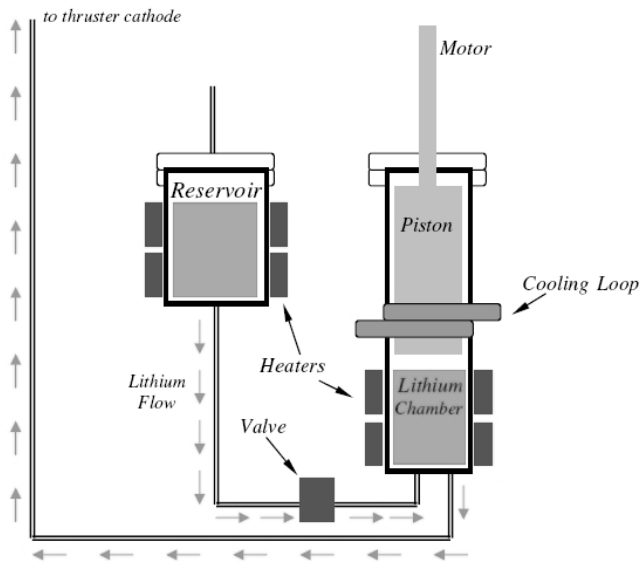

Figure 1. LiLFA Lithium Feed System. Lithium flows from the reservoir to the cylinder where it is pushed by the piston through the pipe line and into the thruster cathode.

B. Lithium Propellant Supply

The lithium is fed through a dedicated feed system that is located in the vacuum chamber and whose design and calibration were discussed by Kodys et. al.[12] Once brought to its melting temperature, lithium flows out of the reservoir and into a cylinder where it awaits ejection by a piston whose position is carefully controlled. Once forced out of the cylinder, liquid lithium flows through a stainless steel 1/4″-pipe to the thruster's cathode where it is vaporized by a heater inside the cathode. The entire feed system requires about 1 kW of electric power and is controlled by four variacs to maintain a temperature of about 250°C during steady-state operation, about 70°C above lithium's melting temperature.

The lithium mass flow rate is directly proportional to the piston's velocity inside the cylinder,[12] and can be varied within a range of 1-200 mg/s. Operation of the thruster itself is accomplished using a 'Miller' SRS-1000 30 kW generator capable of supplying DC current up to 1500 A.

C. The Thruster

The LiLFA (Fig. 2) was built and initially tested at **M**oscow **A**viation **I**nstitute (MAI). It was transferred to Princeton's EPPDyL in 1998. It consists of a conical anode made of tungsten with an upstream inner diameter of 45 mm and a downstream inner diameter of 70 mm. The cylindrical multi-channel hollow cathode (MCHC), also made of tungsten, has an inner diameter of 19.2 mm and a length of 215 mm (100 mm in the thruster cavity). Its tip consists of 68 small rods, each 2 mm in diameter and 14 mm in length. Before thruster initiation the cathode evaporates the incoming liquid lithium provided by the feed system due to high initial temperature of well over 1000°C, maintained by a graphite heater that is embedded inside the cathode and that requires approximately 1.2 kW of power.
During operation the cathode reaches temperatures of well over 2000°C[15] while the anode reaches temperatures of up to 2000°C.[23]
The applied magnetic field is generated by a water cooled solenoid, 280 mm in outer diameter and 120 mm in inner diameter. The solenoid consists of a copper tube 8 mm in diameter which is turned 56 times in order to generate magnetic field values up to 0.08 T with current of 250 A. At this operational point the solenoid requires approximately 2.6 kW of power.

Since no effort was made to optimize the power consumption of the solenoid and lithium feed system, and since that consumption would depend on design considerations that are largely extraneous to the plasma dynamics of the discharge inside the thruster, the required power to operate these supporting subsystems was not included in the calculation of the thrust efficiency reported in this paper. However, we emphasize that in this type of system these additional power consumption requirements will have an effect on the overall system efficiency and must be taken into account in any final engineering design. In the LiLFA system the solenoid and lithium preheating subsystems require about 2 kW each.

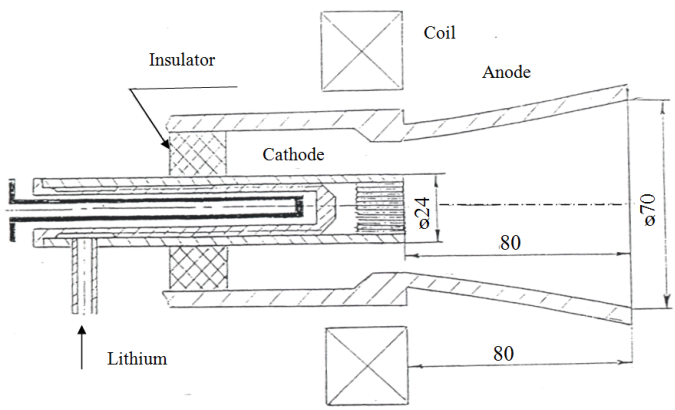

Figure 2. Cross-sectional view of the Lithium Lorentz Force Accelerator (all dimensions are in millimeters).

D. Diagnostics

In this study we measured the floating potential relative to the anode and the anode temperature. The floating potential was measured using an emissive Langmuir probe and the anode temperature was measured by means of an optical pyrometer. Both diagnostics, and their positioning inside the vacuum chamber, are illustrated in Fig. 3.

1. Floating Emissive Probe

A stationary, electrically isolated, floating, emissive Langmuir probe, 1 mm in diameter and 2 mm in exposed length (Fig. 4), was used to measure anode sheath voltage fall by positioning the probe about 1 mm away from the anode wall at the anode face.

The probe tip is made of tungsten wire (1 mm in diameter) encapsulated in a cylindrical ceramic sheath to prevent electron and ion collection outside of the anode region. It is held in place by a steel stand about 25 cm away from the anode so to prevent any interference to potential measurements made by the probe. The probe is not biased and is electrically floating at the potential in the near anode region. It is

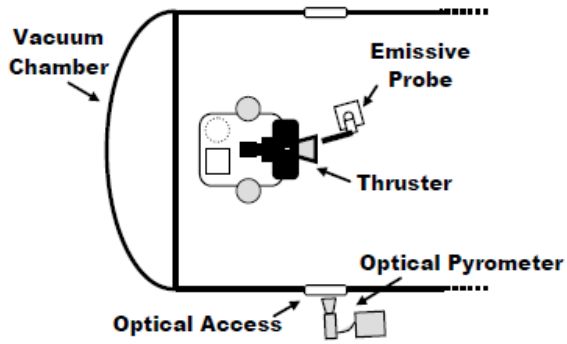

Figure 3. Illustration of the diagnostics layout inside the vacuum chamber.

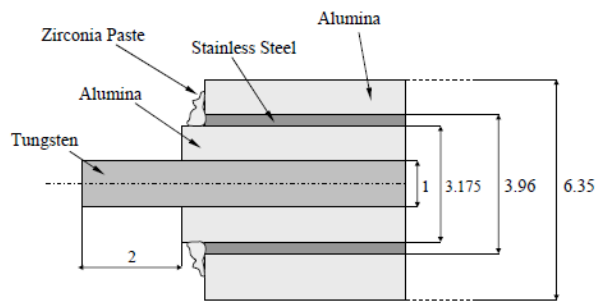

Figure 4. Schematic of the floating Langmuir emissive probe. All dimensions are in millimeters.

exposed to temperatures well over 1600 K, which is required for emitted charge saturation from the probe surface.[16] This ensures a known potential difference of $\Delta_{CL} = 1.23\frac{k_B T_e}{e}$ Volts between the floating and plasma potentials and enables the estimation of the plasma potential relative to anode potential that is the anode sheath voltage fall.[25] The electron temperature in the near anode region can be estimated to be 2 eV as measured at MAI over a wide range of current values.[22]

Anode sheath voltage fall measurements were taken by extending two high-temperature insulated wires from the probe and anode separately, and measuring the voltage between them. All floating potential probe measurements were taken relative to the anode. The measured voltage was then processed by a circuit designed specifically to safely handle and obtain the voltage readings. All data was recorded in real time by the operator and post-processed after the experiment.

2. Optical Pyrometry

A 'Leeds and Northrup' disappearing-filament optical pyrometer, model 8622-C, was used to measure the anode temperature during LiLFA operation. The pyrometer contains a tungsten line filament which is current-heated until it matches, at a wavelength of 650 nm, the brightness of the object the pyrometer is pointed at. The matching is done visually by the operator by raising or lowering the current to the filament thereby changing its emitted intensity. The pyrometer is pre-calibrated such that the heating current in the filament corresponds to a gray-body brightness, with a known emissivity, at 650 nm.

The pyrometer is positioned outside of the vacuum chamber and next to the side glass window with a direct line of sight to the anode, as shown in Fig. 3. The temperature measured by the pyrometer is the brightness temperature and is gray-body-corrected according to Eq. 1

$$T_g = \alpha \left[\ln\left[1 + \epsilon\left(e^{\alpha} - 1\right)\right]\right]. \tag{1}$$

where $\alpha = hc/\lambda k_B$. T_g can be regarded as the temperature at which a gray body with an emissivity ϵ_{eff} has intensity equivalent to a blackbody with a temperature T_b. The emissivity for the anode was taken as the emissivity of tungsten at a temperature of 2000 K, which is $\epsilon = 0.442$.[17] Another correction is required for

the glass window transmissivity, which we take to be $\tau = 0.8$.[4] Therefore the effective emissivity coefficient is $\epsilon_{eff} = 0.442 \times 0.8 = 0.354$.

E. Experimental Conditions

All measurements mentioned above were taken at three different mass flow rates, 5 mg/s, 8 mg/s and 20 mg/s. For each of the three mass flow rates, measurements were taken for applied magnetic field values between 0 T and 0.08 T, and total thruster current values between approximately 100 A and 800 A and within the limits of the power supply. A total of 53 different cases with and without an applied magnetic field were studied. This variety of operational parameters enables a thorough characterization of the anode sheath voltage fall. At each experimental condition data were obtained after langmuir probe voltage reached steady state which usually took about 4 min. All magnetic field values were measured at the center of the solenoid.

Error estimations were made at each measurement for each individual anode voltage fall value according to the estimated voltage fluctuations observed at each reading.

III. Anode Voltage Fall Model Formulation

We start our theoretical formulation by assuming a 1-D model in r for a general AF-MPD thruster as depicted in Fig. 5. We assume a radially constant electron and ion temperatures, T_e and T_i,[10,24] and an unknown radially dependent plasma density, $n_e(r)$, due to plasma pinching. We also assume a constant anode temperature as the anode temperature was found to be approximately uniform at MAI.[21]

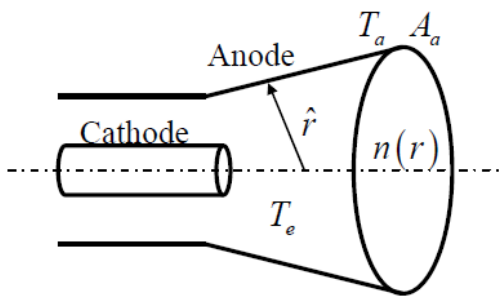

Figure 5. Anode Voltage Fall Model Schematic.

Taking a look at a segment of the anode (Fig. 6), we can write a current density balance equation.[26]

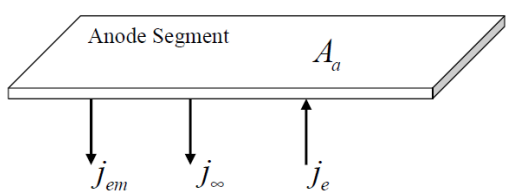

Figure 6. Anode Voltage Fall Model - Current density balance at anode surface.

$$j_\infty = j_e - j_{em}, \tag{2}$$

where j_∞ is the net current density from the anode and can be written as

$$j_\infty = J/A_a. \tag{3}$$

j_e is the electron current density into the anode and can be written as

$$j_e = \frac{1}{4} e n_e \left(\frac{8 k_B T_e}{\pi m_e} \right)^{1/2} e^{\left(\frac{eV_a}{k_B T_e}\right)} \tag{4}$$

where V_a is the anode sheath voltage drop and the electrons are assumed to be Maxwellian. V_a is taken to be the potential increase between the anode sheath and anode wall and is taken here to be positive for convenience. The electron temperature, T_e, in the near-anode region is taken to be 2 eV as measured at MAI over a wide range of current values.[22]
j_{em} is the thermionically emitted electron current density and can be written as

$$j_{em} = A_R T_a^2 e^{(-\frac{e\phi_a}{k_B T_a})} \tag{5}$$

where A_R is the Richardson-Dushman coefficient and is $A_R = 1.2 \times 10^6\ A/m^2K^2$. Eq. 2 indicates that the net current density from the anode is equal to the current density difference between the input electron current density into the anode and the thermionically emitted electrons out from the anode surface. Eq. 2 also implies that at a given total current any increase in thermionically emitted current density will require an increase in the sheath potential drop so to increase the electron current density into the anode.

Solving Eqs. 2-5 for V_a produces

$$V_a = \frac{k_B T_e}{e} \ln \left(\frac{J/A_a + A_R T_a^2 e^{(-\frac{e\phi_a}{k_B T_a})}}{\frac{1}{4} e n_e \left(\frac{8 k_B T_e}{\pi m_e} \right)^{1/2}} \right). \tag{6}$$

Since we are trying to formulate an expression for V_a as a function of the thruster's operational parameters, J, B and $\dot{m}$, we must find an expression for $n_e(J, B_c, \dot{m})$ and $T_a(J, B_c, \dot{m})$.

A. Scaling Relations for Radial Density Profile

We start with $n_e(J, B_c, \dot{m})$ by writing the MHD momentum equation in the radial direction

$$\rho \left[\frac{\partial u_r}{\partial t} + u_r \frac{\partial u_r}{\partial r} + \frac{u_\theta}{r} \frac{\partial u_r}{\partial \theta} + u_z \frac{\partial u_r}{\partial z} - \frac{u_\theta^2}{r} \right] = j_\theta B_z - j_z B_\theta - \frac{\partial P}{\partial r}. \tag{7}$$

We assume steady state operation ($\frac{\partial}{\partial t} = 0$) and azimuthal symmetry ($\frac{\partial}{\partial \theta} = 0$). We also assume that $u_r \simeq 0$ and $\frac{\partial u_r}{\partial z} = 0$ based on the study conducted by Tobari on AF-MPDT[28] where the radial velocity, u_r, was found to be negligible compared with u_θ and u_z and constant radially.
We are now left with the equation

$$-\rho \frac{u_\theta^2}{r} = j_\theta B_z - j_z B_\theta - k_B (T_e + T_i) \frac{\partial n_e}{\partial r}, \tag{8}$$

where $\partial P/\partial r$ was written as $k_B(T_e + T_i)\partial n_e/\partial r$ under the assumption of a constant radial electron and ion temperatures. Eq. 8 represents the balance between the centrifugal forces and density gradient forces pushing the plasma outwards while an electromagnetic pinching effect constrains the plasma inwards towards the centerline.

We now use an order of magnitude analysis to the determine the leading term in Eq. 8 that balances the density gradient term on the RHS. To do so, we use the data reported by Tobari[28] since it is the only source that includes measurements of both u_θ and j_θ that are required for this analysis. The typical values reported by Tobari are presented in Table 1.

We see from Table 1 that the centrifugal forces can be omitted and the density gradient term balances the electromagnetic pinching term. Eq. 8 can now be written as

$$k_B (T_e + T_i) \frac{\partial n_e}{\partial r} = j_\theta B_z - j_z B_\theta = f_r \left(n_e, r, J, B, \dot{m} \right). \tag{9}$$

Here $f_r \left(n_e, r, J, B, \dot{m} \right)$ is the radial force density upon which we will elaborate thoroughly below.

To find $n_e(J, B, \dot{m})$ from Eq. 9, one has to find $j_\theta(r, n_e, J, B, \dot{m})$, $j_z(r, n_e, J, B, \dot{m})$ and $B_\theta(r, n_e, J, B, \dot{m})$ which is not a simple task. We avoid this by departing from a purely theoretical description of the plasma density distribution and using a few basic scaling relations derived from our current understanding of MPDT physics. These basic relations will be used to find scaling relations for the plasma density with respect to the operational parameters, which in turn will be used in the anode sheath voltage fall model. Therefore, the anode sheath voltage fall model will not be purely theoretical. However, since our ultimate goal is to

Property	*Typical Value*
u_θ [m/s]	10^4
r [m]	10^{-2}
ρ $[kg/m^3]$	10^{-7}
j_θ $[A/m^2]$	2×10^6
B_z [T]	2×10^{-2}
$\rho u_\theta^2/r$ $[N/m^3]$	10^3
$j_\theta B_z$ $[N/m^3]$	4×10^4

Table 1. Typical values of plasma properties in AF-MPDT for order-of-magnitude analysis for the pressure balance equation

find and understand trends in anode sheath voltage fall as it varies with the operational parameters, it will be sufficient for our purpose to use these scaling relations and compare them to the trends observed in the anode sheath voltage fall data. From the comparison to the experimental data conclusions and physical insights will be drawn.

We start by acknowledging that $f_r = (\bar{j} \times \bar{B})_r = j_\theta B_z - j_z B_\theta$ represents the radial force density acting to pinch the plasma fluid. The radial force density, $f_r\left(n_e, r, J, B, \dot{m}\right)$, was theoretically shown by Jahn[8] in self-field MPD thrusters to scale in the same manner as thrust, $\mathcal{T}$, with respect to operational parameters; that is they scale with J^2. The reasoning for the relation between f_r and thrust in self-field MPDTs stems from the fact that the axial current density, j_z, and the self-induced azimuthal magnetic field, B_θ, both scale linearly with current, J. We expect the same relation between f_r and $\mathcal{T}$ to exist in AF-MPDTs where thrust was shown to be produced mainly by plasma pinching.[28] In addition, since $\mathcal{T}$ was experimentally shown[11] in AF-MPD thrusters to scale with the product JB we will write the general expression for thrust generated by pinching as $\left(A_1 J B_c + A_2 J^2\right)$ where A_1 and A_2 are proportionality constants. Therefore, we can make the assumption that f_r in AF-MPDTs is proportional to $\left(A_1 J B_c + A_2 J^2\right)$.

This scaling relation is not sufficient for the characterization of f_r and a solution of Eq. 9 since it lacks the spatial dependence of f_r on radial position; simply put, $f_r = f_r(r)$. This dependency originates from the spatial distribution of the current densities, j_z and j_θ. We will find this spatial dependence by using the steady-state generalized Ohm's law in θ:

$$E'_\theta = \frac{j_\theta}{\sigma_0} + \frac{1}{n_e e}\left(j_z B_r - j_r B_z\right), \tag{10}$$

where $E'_\theta = E_\theta + u_z B_r - u_r B_z + \frac{1}{n_e e}\partial P_e/\partial\theta$. We make the assumption that the electric field is purely radial in the interelectrode region ($E_\theta = 0$) and that due to symmetry $\partial/\partial\theta = 0$. We also make the assumption that the applied axial magnetic field, B_z, is dominant thus $B_\theta = B_r = 0$. By applying the above assumptions we arrive at

$$-u_r B_z = \frac{j_\theta}{\sigma_0} + \frac{1}{n_e e}\left(-j_r B_z\right). \tag{11}$$

We make the assumption that the radial electron current density dominates the total radial current density due to the large ion mass, that is $j_r/n_e e \gg u_r$. We also use the expression for the scalar conductivity, $\sigma_0 = n_e e^2/(m_e \nu_e)$ and $\Omega_e = \frac{eB_z}{m_e \nu_e}$ which is the electron Hall parameter. Eq. 11 can be written as follows:

$$j_\theta = \Omega_e j_r. \tag{12}$$

Eq. 12 shows the basic relation between current flowing parallel to the electric field, and the induced current, the Hall current, perpendicular to the electric field. Both currents are perpendicular to the magnetic field lines. This mathematical process was previously presented by Tikhonov,[3] Krülle[13] and Tobari.[28] We will use this relation shortly.

We now write the steady-state generalized Ohm's law in r:

$$E'_r = \frac{j_r}{\sigma_0} + \frac{1}{n_e e}\left(j_\theta B_z - j_z B_\theta\right), \tag{13}$$

where $E'_r = E_r + u_\theta B_z - u_z B_\theta + \frac{1}{n_e e}\partial P_e/\partial r$. To simplify Eq. 13 we make the assumption that the applied axial magnetic field, B_z, is dominant thus $B_\theta = B_r = 0$. We also make the assumption that the electric field due to radial electron density gradient, $\frac{1}{n_e e}\partial P_e/\partial r$, is negligible compared to the applied electric field, E_r similar to Krülle[13] and Lev.[16] Eq. 13 can now be rewritten as:

$$E_r + u_z B_\theta = \frac{j_r}{\sigma_0} + \frac{1}{n_e e}\left(j_\theta B_z\right). \tag{14}$$

We assume that the azimuthal current density, j_θ, is dictated by electron motion. This assumption can be supported by examining the typical values of u_θ and j_θ presented in Table 1. From the table it can be concluded that j_θ/en_e is about two orders of magnitude higher than u_θ, for $en_e \simeq 1$. Rearranging Eq. 14 and using the relation derived earlier, $j_\theta = \Omega_e j_r$, we arrive at:

$$j_\theta = \sigma_0 \frac{\Omega_e}{1+\Omega_e^2} E_r. \tag{15}$$

This expression presents the relation between the radial electric field and the azimuthal current density component perpendicular to the applied magnetic field. This process was previously derived and presented in AF-MPDTs by krülle.[13]

Now that we have an expression for j_θ we can go back to the sought $f_r(r)$ while assuming that the dominant radial force component responsible for the radial density distribution is mainly due to the applied field ($f_r \simeq j_\theta B_z$). By using this assumption the radial force density can be written as

$$f_r = j_\theta B_z = \sigma_0 \frac{\Omega_e}{1+\Omega_e^2} B_z E_r \simeq \sigma_0 \frac{1}{\Omega_e} B_z E_r = n_e e E_r, \tag{16}$$

where we used the fact that in AF-MPDTs $\Omega_e \gg 1$.[6,14,18] Eq. 16 gives the relation between f_r and E_r and should technically be sufficient for solving Eq. 9, however, the value of E_r is not known since it depends on the total voltage and anode sheath voltage fall which are unknown. For this reason we only use the spatial dependence of E_r that was measured experimentally by Tobari[28] and Ando[2] to be linear with radial position ($E_r = E_0 r$). Therefore, the spatial dependence of $f_r(r)$ is $f_r(r) \propto n_e(r) r$.

This scaling relation comes in accordance with measurements taken by Tobari in AF-MPDTs[28] that demonstrated the radial force density to be largest at the thruster's centerline and to decrease radially.

We can therefore assume that $f_r = \left(C_1 J B_c + C_2 J^2\right) n_e(r) r$ where the constants C_1 and C_2 are to be determined from fitting the expression for V_a to experimental data presented in section IV.

Although this expression for f_r was derived in a somewhat qualitative manner, it still captures the fundamental dependence of the radial force density, f_r, on the operational parameters and plasma density. We must remember that our objective is to characterize the basic scaling relations of n_e at the anode region in order to find a scaling relation for V_a. These will be used to pursue similarities between the modeled V_a and the observed trends from the data.

We can now write Eq. 9 in the form of an ordinary differential equation in r

$$\frac{\partial n_e}{\partial r} = -(C_1 J B_c + C_2 J^2) n_e r \tag{17}$$

with the boundary condition $n_{e,r=0} = n_{e,0}$. In Eq. 17 the term $k_B(T_e + T_i)$ was absorbed into the constants C_1 and C_2 since it is assumed to be constant.

Since $\dot{m} = \rho A u = n_e m_i A u$ we will write $n_{e,0} = C_3 \dot{m}$ which means that as the mass flow rate to the thruster is increased so is the density at the thruster's centerline. Eq. 17 has the solution

$$n_e(r) = C_3 \dot{m} e^{-(C_1 J B_c + C_2 J^2) r^2}. \tag{18}$$

It can be seen from the radial density profile, $n_e(r)$, that the density decreases with radial position which implies a density reduction closer to the anode. This Gaussian density profile was observed in AF-MPDTs by Ando.[2] Similarly, in self-field MPDTs a density reduction of a few orders of magnitude was observed in the near anode region by Gallimore,[6] Saber[24] and Tilley.[27] In addition, it can be seen from the radial density profile, $n_e(r)$, that an increase in J and B_c leads to a stronger decrease in n_e with r. In simple words, an increase in J and B_c pinches the plasma towards the thruster's centerline as postulated earlier. We also see that an increase in $\dot{m}$ will lead to an increase in density at all radial positions. This was also expected since any addition of propellant is expected to increase the number of particles, at all locations in the thruster, thus increasing n_e.

The expression for $n_e(r)$ can now be used in the formulation for the anode voltage fall, V_a, given in Eq. 6.

B. Empirical Formulation of Anode Temperature

To analytically obtain an expression for $T_a(J, B, \dot{m})$ one has to solve the anode power balance equation which requires knowledge of the cathode temperature due to its strong contribution to anode power balance. Since the cathode temperature and its dependence on the operation parameters is unknown we do not attempt to solve the anode power balance equation. To find $T_a(J, B, \dot{m})$ we use an empirical formulation based on anode temperature data obtained from LiLFA operation at a variety of operational parameters regimes as described in section II. The best mathematical form that could be fit to the anode temperature data is

$$T_a(J, B, \dot{m}) = 1080 + 2375B_c - 5 \times 10^6\dot{m} + (1.366 - 1.33 \times 10^4\dot{m})J. \tag{19}$$

Figs. 7-9 show the anode temperature change with respect to current at different applied magnetic fields and mass flow rate values with the empirical fit according to Eq. 19. It can be seen that the empirical fit

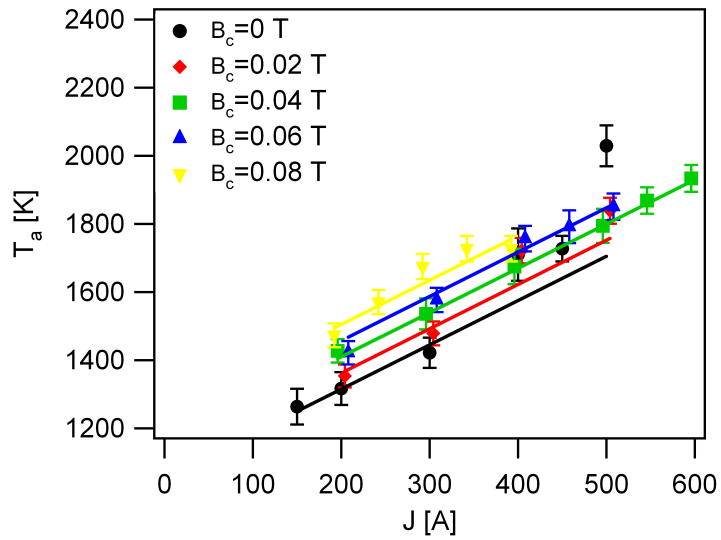

Figure 7. Anode Temperature vs. Current for different applied magnetic field values at $\dot{m}$=5 mg/s. The solid lines represent the empirical fit according to Eq. 19 for applied field values in the range 0-0.08 T.

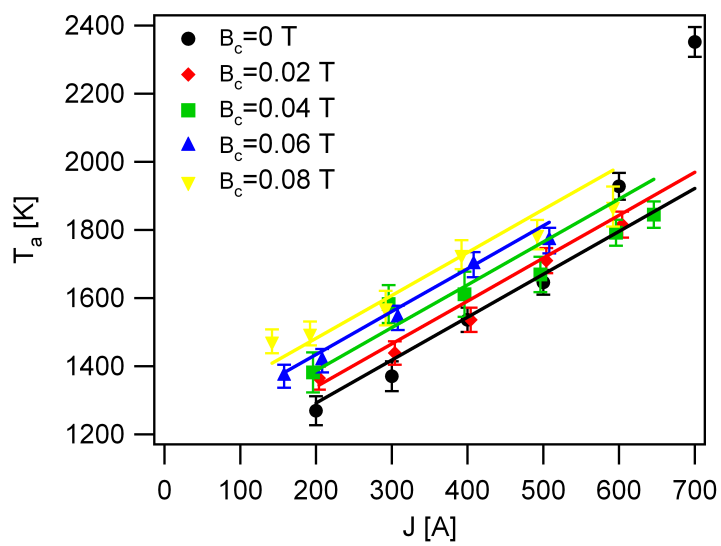

Figure 8. Anode Temperature vs. Current for different applied magnetic field values at $\dot{m}$=8 mg/s. The solid lines represent the empirical fit according to Eq. 19 for applied field values in the range 0-0.08 T.

agrees with most data to within the error bars. It can also be observed from the anode temperature data that the strongest dependence of anode temperature is on current and with only a weak dependence on the

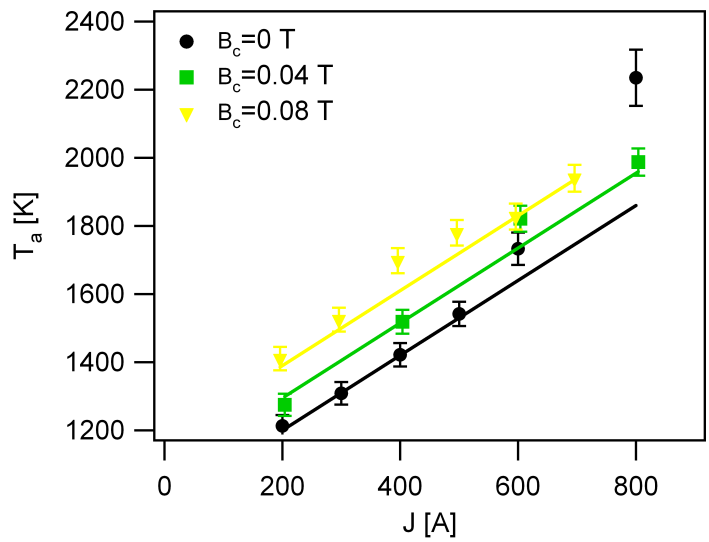

Figure 9. Anode Temperature vs. Current for different applied magnetic field values at $\dot{m}$=20 mg/s. The solid lines represent the empirical fit according to Eq. 19 for applied field values in the range 0-0.08 T.

applied magnetic field and mass flow rate. Therefore, for the simplicity of the scaling relations analysis we will assume that the anode temperature is approximately linearly dependent only on current.

The expression for $T_a(J, B_c, \dot{m})$ can now be used in the expression for the anode voltage drop, V_a, given in Eq. 6.

IV. Solution and Comparison to Experimental Data

Using Eq. 6, Eq. 18 and Eq. 19 we have a complete expression for the anode sheath voltage fall, V_a, as a function of the operational parameters, J, B_c and $\dot{m}$. The full expression is not presented here due to its length. This expression gives the basic scaling laws for anode sheath voltage fall and assists in understanding the fundamental physics behind this power dissipation mechanism. To verify these scaling laws we compare them to experimental data of anode voltage fall obtained from LiLFA operation as described in section II, and show that V_a exhibits the same mathematical trends with changing current, applied field and mass flow rate.

Figs. 10-12 show the anode sheath voltage fall data along with curves fit according to Eq. 6. The constants in the expression (Eq. 18) for the plasma density, $n_e(r)$, used are $C_1 = 0.19$, $C_2 = 2\times10^{-6}$ and $C_3 = 2\times10^{21}$ and were found from fitting the curves to the experimental data at B_c=0.04 T and $\dot{m}$=8 mg/s.

It can be seen from the figures that the semi-empirical anode voltage fall model predicts the trends in the measured data fairly well. At $\dot{m}$=5 mg/s the semi-empirical model matches the measured values at B_c=0.08 T and is close to the values of the case B_c=0 T. At the same time the model under-predicts the data for the case of B_c=0.04 T. The deviation from the measured data might be attributed to the onset phenomenon at higher current values where the anode overheats and thermionically emits higher electron current density out from its surface. This current density is countered by a larger incoming electron current density due to an increasing voltage fall. This phenomenon occurs at low mass flow rates as in our case. At $\dot{m}$=8 mg/s the semi-empirical model matches the data points very well. At $\dot{m}$=20 mg/s the model predicts the measured data quite well except for at high current values at B_c=0.08 T. We can attribute this behavior to an underestimation of the plasma density at high current, applied magnetic field and mass flow rate. It is possible that at high mass flow rate centrifugal forces push the plasma from the thruster's center outwards while increases the density in the near anode region. Since centrifugal force density was omitted from our derivation of n_e this effect is not taken into account. Nevertheless, the trends in predicting V_a at $\dot{m}$=20 mg/s and B_c=0.08 T are still captured.

In general, the semi-empirical anode voltage fall model captures the trends observed from the measured data. The model predicts an increase in anode voltage fall with increasing current and applied magnetic field

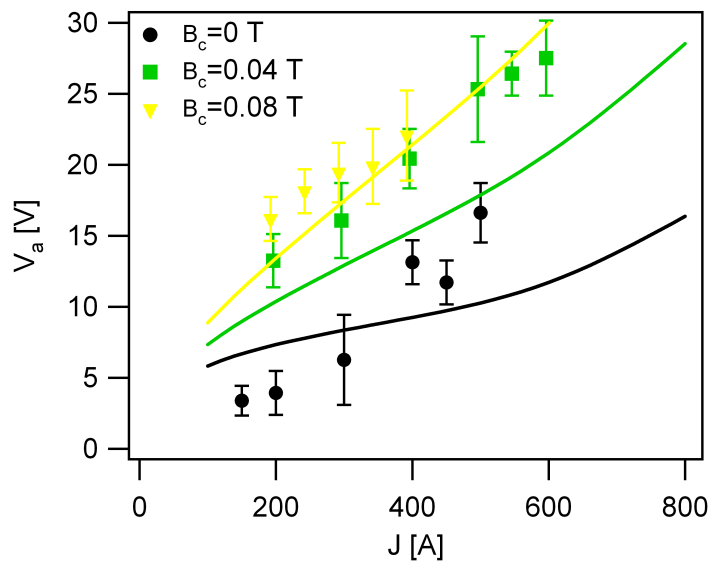

Figure 10. Anode sheath voltage fall vs. current for different applied magnetic field values at $\dot{m}$=5 mg/s. The solid lines represent the semi-empirical fit according to Eq. 6 for applied field values in the range 0-0.08 T.

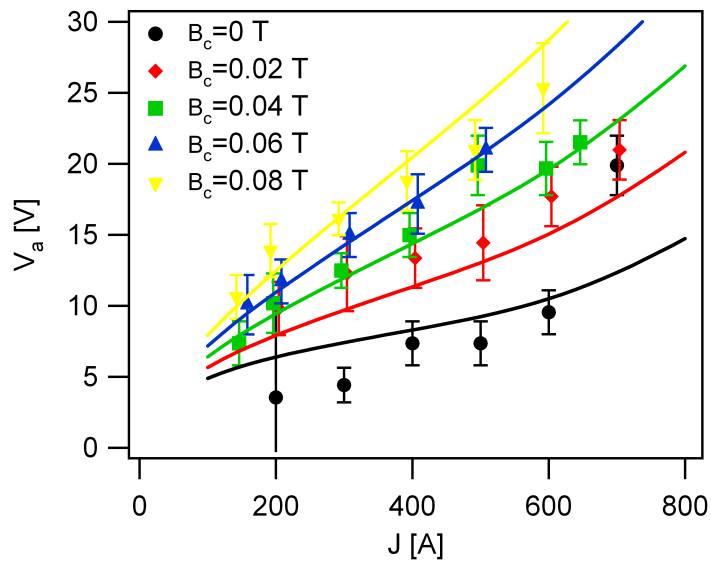

Figure 11. Anode sheath voltage fall vs. current for different applied magnetic field values at $\dot{m}$=8 mg/s. The solid lines represent the semi-empirical fit according to Eq. 6 for applied field values in the range 0-0.08 T.

while predicting a mild decrease in anode voltage fall with increasing mass flow rate. The linear increase of anode voltage with current was observed in previous studies in MPDTs.[6,29] The model also estimates a sharper increase of V_a with current at higher applied field values although this trend is not observed in all measured data.

V. Physical Interpretation

The scaling relations derived and verified elucidate on the physical mechanisms behind anode sheath voltage fall in AF-MPD thrusters. The value of the anode voltage fall is determined by current density balance at the anode surface. This balance is influenced by total thruster current, plasma density at the near-anode region, anode temperature and thruster geometry.

The dependence of anode sheath voltage fall on the three operational parameters can be explained based

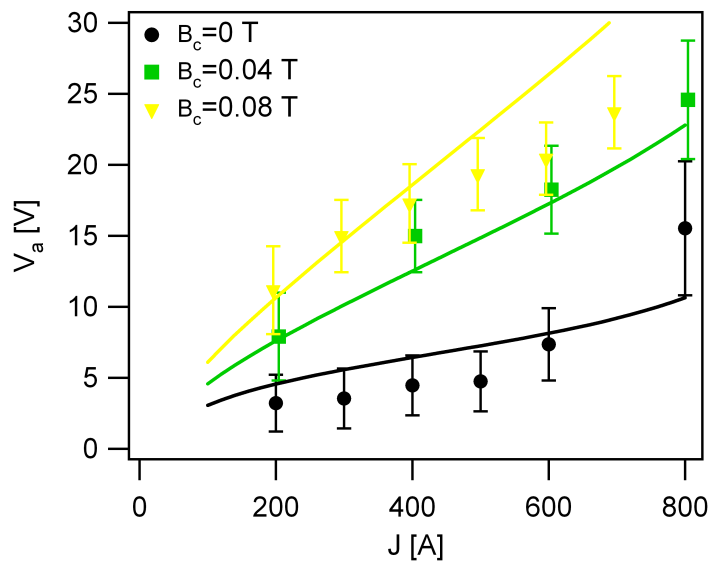

Figure 12. Anode sheath voltage fall vs. current for different applied magnetic field values at $\dot{m}$=20 mg/s. The solid lines represent the semi-empirical fit according to Eq. 6 for applied field values in the range 0-0.08 T.

on Eq. 6.

- Any increase in total thruster current, J, will increase the demand for higher electron current density into the anode which, in turn, will increase the necessary sheath voltage fall in order to meet this demand. An increase in current will also lead to anode heating which will lead to an increase in the thermionically emitted electron current density and will require an increase in sheath voltage fall to compensate for the emitted electron flux. Finally, an increase in thruster current will cause an increased plasma pinching that will cause density reduction at the anode surface and will reduce the random electron flux into the anode. This reduction in electron flux will require an increased sheath voltage fall to maintain current density balance at the anode surface. From Figs. 10-12 we conclude that the dependence of anode sheath voltage fall is approximately linear.

- Any increase in applied magnetic field, B_c, will increase the plasma pinching that will cause density reduction at the near-anode region and will reduce the random electron flux into the anode. This reduction will be compensated by an increase in the sheath voltage fall to maintain current density balance into the anode. This indirect effect of the applied magnetic field on the anode sheath voltage fall explains the dependence of one on the other although the electrons in the anode sheath are unmagnetized. This dependence of the anode sheath voltage fall on the applied magnetic field is approximately linear. This finding corroborates Mayers and Gallimore findings.

- Any increase in mass flow rate, $\dot{m}$, will lead to an increase in plasma density in the near-anode region which will increase the random electron flux into the anode. This increase will lead to a decrease in anode sheath voltage fall to maintain current density balance into the anode. This dependence is weaker than the dependence on J and B_c and has the form $V_a \propto \ln(1/\dot{m})$.

Fig. 13 presents the balance between the three current density components at the anode surface according to Eq. 2. It can be seen from the figure that at low current values the thermionic emission is insignificant and the random electron current density into the anode balances the net current density dictated by the total current to the thruster. As the current to the thruster is increased so does the anode temperature until thermionic emission becomes significant and a larger random electron flux into the anode is required to compensate for the increasing thermionic emission. We can conclude that thermionic emission and anode temperature play important roles in the current density balance in AF-MPDTs and strongly affect anode sheath voltage fall at high current operation.

Thermionic emission from the anode surface has implications on research conducted on quasi-steady MPDTs since the pulse length of these thrusters is too short to allow the anode temperature to reach

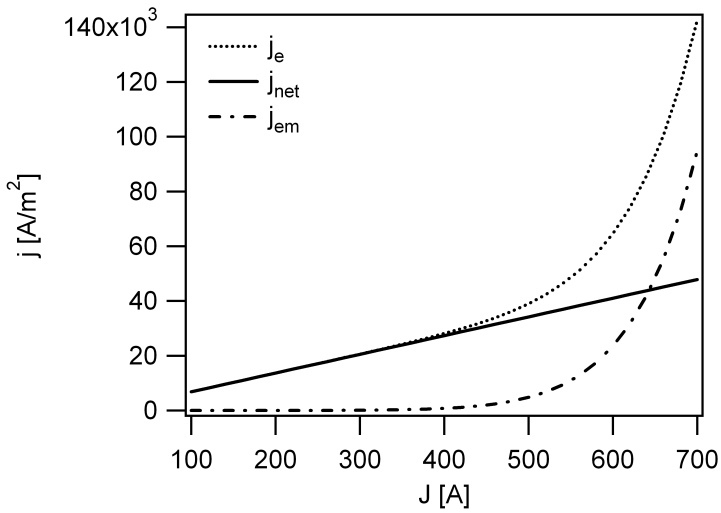

Figure 13. The three current density components (j_e, j_∞, j_{em}) presented in Eq. 2 as a function of total current, J, at B_c=0.04 T and $\dot{m}$=5 mg/s.

steady-state. To support the above statement we conduct a first order estimation of the anode heating time scale and show that it is larger than the average pulse length of high power quasi-steady MPDTs.

The relation between the anode thermal properties and the thruster power is

$$P_a = \frac{C_p m \Delta T}{\Delta t}. \tag{20}$$

Where P_a is the power to the anode, C_p is the anode material heat capacity, m is the anode mass, ΔT is the temperature difference between room temperature and effective anode surface emission temperature and Δt is the heating time. We use the typical values for a high power quasi-steady MPDTs: $P_a \simeq 10^6$ W, $C_p \simeq 200$ J/kg K, $m \simeq 3$ kg and $\Delta T \simeq 1500$ K. The solution of Eq. 20 is $\Delta t = 0.9$ sec which is the time scale for anode heating to 2000 K in a quasi-steady MPDT. Quasi-steady MPDT pulse length is usually in the range $\Delta t_{pulse} \simeq 1$ millisec which is about three orders of magnitude shorter. We can therefore conclude that the anode in a typical quasi-steady MPDT has no time to reach a temperature range that is sufficient for thermionic emission to have a significant effect on the anode sheath voltage fall, V_a.

VI. Conclusions

A semi-empirical anode sheath voltage fall model was derived to find scaling relations with the thruster's operational parameters, J, B_c, $\dot{m}$, and reveal the physical mechanisms behind anode power dissipation in AF-MPDTs. The model was successfully verified against measured data and was found to predict the observed trends of the anode voltage fall with the operational parameters.

The semi-empirical model has allowed us to achieve the following physical insights.

- **The anode sheath voltage fall increases with increasing current, J.** The random electron current density through the sheath must increase when total current to the thruster increases. To achieve this increase the anode fall has to increase so to draw more electrons through the sheath. In addition, an increase in total current increases the plasma pinching thus reducing the density in the near anode region which in turn reduces the electron current density through the sheath. This density reduction requires a larger voltage fall to attract more electrons through the sheath.

  It is important to note that this increase in anode voltage fall is approximately linear with current ($V_a \propto J$).

- **The anode sheath voltage fall increases with increasing applied field, B_c.** An increase in the applied magnetic field leads to an increase of the pinching force towards the thruster's centerline which in turn decreases the density in the near anode region. This decrease in density reduces the

electron current density through the sheath and requires a larger sheath voltage fall for attracting more electrons through the sheath. It should be noted that even though the electrons are not magnetized in the anode sheath the applied magnetic field affects the sheath potential fall indirectly by increasing the plasma pinching and reducing the plasma density at the sheath.

It is also important to note that much like the increase with current the anode voltage fall seems to be linear with applied magnetic field ($V_a \propto B_c$).

- **The anode sheath voltage fall decreases with increasing mass flow rate, $\dot{m}$.** Propellant mass flow rate affects the anode sheath voltage fall by affecting the density in the near anode region. An increase in mass flow rate leads to an increase in density which in turn increases the electron current density into the anode. When the electron current density into the anode is larger, a lower sheath voltage is required to maintain the same total current. The anode voltage fall has a weak dependence on the mass flow rate ($V_a \propto \ln(1/\dot{m})$).

- **Thermionic emission from the anode has an effect on the anode sheath voltage fall.** Using our model we have shown that thermionic emission from the anode surface is responsible for reducing the net current density into the anode and increasing the required anode sheath voltage fall to maintain current density balance at the anode surface. This fact has important design implications on the choice of anode material since it is desirable to reduce anode thermionic emission by choosing materials with high work function values. In addition, this conclusion has implications on testing and experimentation of MPDTs since quasi-steady operation does not exhibit the anode thermal effects due to the short operation time. Therefore steady-state operation of MPDTs should be preferable for power balance examination such as in the study of thrust efficiency to best capture the anode thermal effects that tend to increase the anode power requirements.

  Finally, this phenomenon was observed in high power arcjets by Golz[7] who found the total thruster voltage to be lower at the same operating conditions when the anode was water-cooled. It is possible that the lower voltage is due to lower thermionic emission and so to lower required sheath voltage fall.

Acknowledgments

We acknowledge the support of the Plasma Science and Technology Program from the Princeton Plasma Physics Laboratory, the help of Dr. Yevgeny Raitses and the technical help of Mr. Robert Sorenson.

References

[1] V.P. Ageyev and V.G. Ostrovsky. High current stationary plasma accelerator of high power. In *The 23th International Electric Propulsion Conference (IEPC), 1993, Seattle, WA, IEPC-93-117*, 1993.

[2] Ando Akira, Ashino Masashi, Sagi Yukiko, Inutake Masaaki, Hattori Kunihiko, Yoshinuma Mikirou, Imasaki Atsushi, Tobari Hiroyuki, and Yagai Tsuyoshi. Spectroscopic studies of a high mach-number rotating plasma flow. *J. Plamsa Fusion Res.*, 4:373–378, 2001.

[3] M. Andrenucci. *Magnetoplasmadynamic Thrusters.* Wiley, Online Library, 2010.

[4] Newport Corporation. Tranmittance of optical materials, May 2011.

[5] Kevin D. Diamant. *The Anode Fall in a High Power Pulsed MPD Thruster.* PhD thesis, Princeton Univ., 1996.

[6] Alec Damian Gallimore. *Anode Power Deposition in Coaxial MPD Thrusters.* PhD thesis, Princeton Univ., 1992.

[7] T.M. Golz, M. Auweter-Kurtz, H. Habiger, and H.L. Kurtz. High specific impulse performance of a 100 kw radiation cooled thermal arcjet thruster. In *The 30th Joint Propulsion Conference (JPC), June 27-29, 1994, Indianapolis, IN. AIAA-94-3249*, 1994.

[8] R.G. Jahn. *Physics of Electric Propulsion.* McGraw-Hill, New York, 1968.

[9] J.E.Polk and T.J. Pivirotto. Alkali metal propellants for MPD thrusters. In *AIAA/NASA/OAI Conference on Advanced SEI Technologies, September 4-6, 1991, Cleaveland, OH. AIAA-91-3572*, 1991.

[10] A. J. Kelly, N. M. Nerheim, and J. A. Gardner. Electron density and temperature measurements in the exhaust of an MPD source. *AIAA Journal*, 4(2):291–295, 1966.

[11] A.D. Kodys and E.Y. Choueiri. A critical review of the state-of-the-art in the performance of applied-field magnetoplasmadynamic thrusters. In *The 41st Joint Propulsion Conference (JPC), July 10-14, 2005, Tucson, AZ. AIAA-2005-4247*, 2005.

[12] A.D. Kodys, G. Emsellem, L.D. Cassady, J.E. Polk, and E.Y. Choueiri. Lithium mass flow control for high power lorentz force accelerators. Technical report, Princeton Univ., Princeton, NJ, USA, Jet Propulsion Lab, Pasadena, CA, 2001.

[13] G. Krülle. Characteristics and local analysis of mpd thruster operation. In *AIAA Electric Propulsion Conference, September 11-13, 1967, Colorado Springs, CO, 67-672*, 1967.

[14]Gerd Krülle, Monika Auweter Kurtz, and Akihiro Sasoh. Technology and application aspects of applied field magnetoplasmadynamic propulsion. *Journal of Propulsion and Power*, 14(5):754–763, 1998.

[15]Cassady L.D. *Lithium-Fed Arc Multichannel and Single-Channel Hollow Cathode: Experiment and Theory*. PhD thesis, Princeton Univ., 2006.

[16]Dan Lev. *Investigation of Efficiency in Applied-Field MagnetoPlasmaDynamic Thrusters*. PhD thesis, Princeton Univ., 2011 (to be published).

[17]David R. Lide. *CRC Handbook of Chemistry and Physics, 77th Edition*. National Institute of Standards and Technology, 1997.

[18]P.G. Mikellides and P.J. Turchi. A theoretical model for the thrust and voltage of applied-field MPD thrusters. In *The 34th Joint Propulsion Conference (JPC), July 13-15, 1998, Cleveland, OH. AIAA-94-3474*, The Ohio State University, Columbus, Ohio, USA, 1998.

[19]Roger M. Myers, Alex D. Gallimore, and R.G.Jahn. Anode power deposition in an applied-field segmented anode MPD thruster. *Journal of propulsion and power*, 10(2):262–268, 1994.

[20]Roger M. Myers and George C. Soulas. Anode power deposition in applied-field MPD thrusters. In *The 28th Joint Propulsion Conference (JPC), July 6-8, 1992, Nashville, TN. AIAA-92-3463*, 1992.

[21]G. Popov, V. Kim, V.B. Tikhonov, and S. Semenikhin. The first quarterly report on the stage no 3 a of the contract on the research studies no nasw-4851 between RIAME MAI and NASA. Technical report, Moscow Aviation Institute (MAI), Moscow, Russia, April 1996.

[22]G. Popov, V. Kim, V.B. Tikhonov, and S. Semenikhin. The second quarterly report on the stage no 3 c,d of the contract on the research studies no nasw-4851 between RIAME MAI and NASA. Technical report, Moscow Aviation Institute (MAI), Moscow, Russia, April 1997.

[23]G. Popov, V. Kim, V.B. Tikhonov, and S. Semenikhin. The second quarterly report on the stage no 3 b of the contract on the research studies no nasw-4851 between RIAME MAI and NASA. Technical report, Moscow Aviation Institute (MAI), Moscow, Russia, December 1996.

[24]Aaron Jaan Saber. *Anode Power in the Quasi-Steady MPD Thruster*. PhD thesis, Princeton Univ., 1974.

[25]Roman Schrittwieser, Jiri Adamek, Petru Balan, Martin Hron, Cordina Ionita, Karel Jakubka, Ladislav Kryska, Emilio Martines, Jan Stockel, Milan Tichy, and Guido Van Oost. Measurements with an emissive probe in the castor tokamak. *Plasma Phys. Control. Fusion*, 44:567–578, 2002.

[26]V. V. Subramaniam and J. L. Lawless. Thermal instabilities of the anode in a magnetoplasmadynamic thruster. *J. Propulsion*, 6(2):221–224, 1990.

[27]D. L. Tilley, S. Castillo, M. S. Jolly, E. Niewood, and M. Martinez-Sanchez. A comparison of theory and measurements in the anode region of a self-field cylindrical mpd thruster. In *The 30th Joint Propulsion Conference (JPC), June 27-29, 1994, Indianapolis, IN. AIAA-94-3249*, 1994.

[28]H. Tobari, A. Ando, M. Inutake, and Kunihiko Hattori. Characteristics of electromagnetically accelerated plasma flow in an externally applied magnetic field. *Phys. Plasmas*, 14, 2007.

[29]Daniel D. Villani. *Energy Loss Mechanisms in a Magnetoplasmadynamic Arcjet*. PhD thesis, Princeton Univ., 1982.